Monolithic SiC supports with tailored hierarchical porosity for molecularly selective membranes and supported liquid-phase catalysis

Portela, Raquel; Marinkovic, Jakob Maximilian; Logemann, Morten; Schörner, Markus; Zahrtman, Nanette; Eray, Esra; Haumann, Marco; García-Suárez, Eduardo Jose; Wessling, Matthias; Ávila, Pedro

Total number of authors:
12

Published in:
Catalysis Today

Link to article, DOI:
10.1016/j.cattod.2020.06.045

Publication date:
2022

Document Version
Peer reviewed version

Monolithic SiC Supports with Tailored Hierarchical Porosity for Molecularly Selective Membranes and Supported Liquid-Phase Catalysis

Raquel Portela[1,γ,*], Jakob Maximilian Marinkovic[2,γ], Morten Logemann[3], Markus Schörner[4], Nanette Zahrtman[2,5], Esra Eray[5], Marco Haumann[4], Eduardo J. García-Suárez[2,θ], Matthias Wessling[3,6], Pedro Ávila[1], Anders Riisager[2], Rasmus Fehrmann[2]

1 Institute of Catalysis and Petrochemistry (ICP-CSIC). Spectroscopy and Industrial Catalysis group. C/ Marie Curie, nº2.Cantoblanco, Madrid, Spain

2 Technical University of Denmark, Centre for Catalysis and Sustainable Chemistry, Department of Chemistry, Kemitorvet Building 207, 2800 Kgs. Lyngby, Denmark

3 RWTH Aachen University, Chemical Process Engineering, Forckenbeckstr. 51, 52074 Aachen, Germany

4 Friedrich-Alexander-Universität Erlangen-Nürnberg (FAU), Lehrstuhl für Chemische Reaktionstechnik (CRT), Egerlandstr. 3, 91058 Erlangen, Germany

5 LiqTech International A/S, Industriparken 22C, 2750 Ballerup, Denmark

6 DWI - Leibniz Institute for Interactive Materials, Forckenbeckstr. 50, 52074 Aachen, Germany

θ present address: a)Tecnalia, Parque Tecnológico de Álava, Leonardo Da Vinci Kalea, 11, 01510 Miñano (Araba), Spain; b) IKERBASQUE, Basque Foundation for Science, Maria Diaz de Haro 3, 48013, Bilbao, Spain

γ both authors contributed equally to this work

Corresponding author: raquel.portela@csic.es

Keywords

Silicon carbide; monolith; porosity; molecularly selective membrane; hydroformylation; catalysis

Abstract

Monolithic support materials with the mechanical resistance and thermal conductivity of SiC as well as tunable surface chemistry and textural properties were developed for their use in catalytic membrane reactors. After heat treatment, the extruded SiC monoliths have a monomodal distribution of macropores of a few µm in diameter depending on the particle size of the starting material. A macroporous, defect-free, smoother skin was applied onto the external wall using a solution of sub-micrometer SiC particles. These monoliths with skin could be coated successfully with molecularly selective membranes, and thus have application in membrane reactor processes. Finally, metal oxide nanoparticles were infiltrated into the macropores to modify the surface texture and chemistry, allowing the immobilization of liquid phase catalysts. The resulting multimodal distribution of pore sizes could be tuned by the choice of SiC and oxide particle sizes, number of wash-coats and calcination temperature. Mesopores created between nanoparticles had diameters of roughly 40 % of those of the nanoparticles. Small macropores, between 10-1000 nm, were also created, with bigger size and volume at higher calcination temperatures due to the metal oxide particles contraction. The developed materials were validated as support for PDMS membranes and for continuous gas-phase hydroformylation of 1-butene using Rh-diphosphite catalysts.

1 Introduction

Homogeneous catalysts offer several advantages compared to their heterogeneous counterparts, especially concerning specific activity and overall selectivity. However, the tedious separation of the liquid catalyst complexes from the – usually – liquid reaction mixture hampers the industrial implementation of many promising catalysts [1]. To overcome this setback, several strategies for the immobilization or heterogenization of homogeneous catalysts have been employed [2,3]. One very intriguing technique involves the dispersion of thin films of catalytically active liquid solutions over the large inner surface area of porous support materials [4–6]. The resulting

supported liquid-phase (SLP) materials are macroscopically solids, while on the microscopic level the homogeneous catalyst is dissolved in the appropriate liquid environment [7]. In doing so, the least stress is applied to the catalyst, thereby maintaining its activity and – more important – selectivity [2]. SLP systems have received much attention in recent years in the search for greener and more intensified processes [3,8,9]. However, so far, SLP catalysis has predominantly been performed with packed beds using impregnated grains of micro- to millimeter size, which are challenging to upscale due to several reasons, such as a low heat transfer within the catalyst bed or a high-pressure drop over the bed [10,11]. Monolithic reactors, usually made from ceramics, are promising alternatives to conventional packed bed reactors as they allow improved heat management and simple upscaling by their modular design. Other advantages related to their channeled structure with thin walls are that they have less fouling, low void volume, high geometric area per reactor volume as well as short diffusion paths [12]. Furthermore, structured catalysts allow dissociation and, hence, separate optimization of intrinsic kinetics, fluid dynamics, and transport phenomena [13]. Besides, ceramic monoliths can also be employed as support for molecularly selective membranes to perform *in-situ* product separation and improve downstream processing. This work proposes the innovative use of porous monoliths to embed SLP catalytic systems (Figure 1); the monoliths may also incorporate a selective membrane on the external wall to obtain pioneering monolithic membrane reactors.

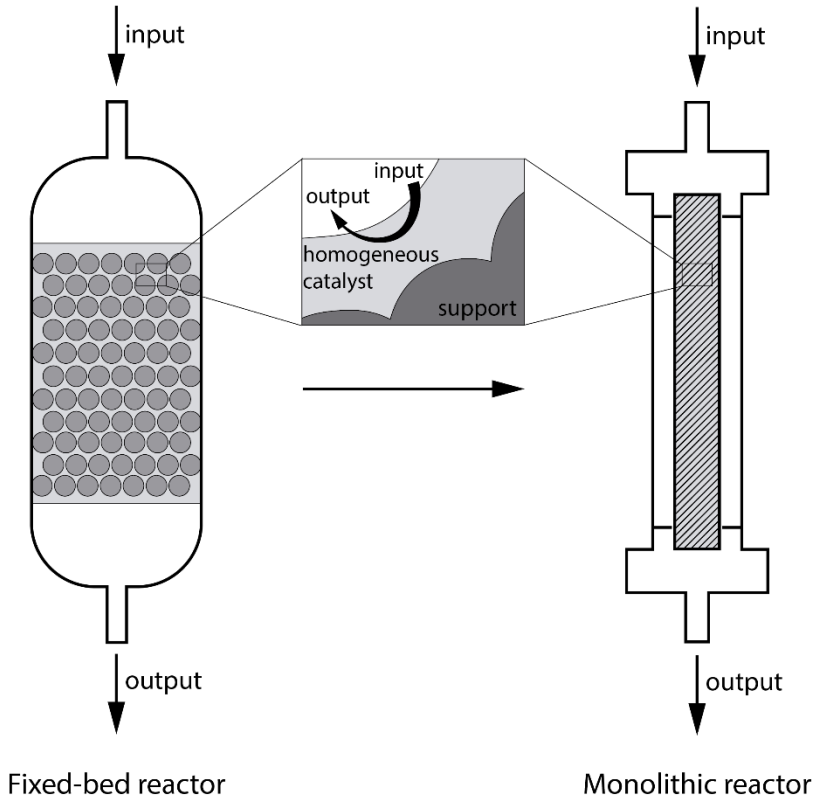

Figure 1. From SLP in fixed-bed reactors to SLP in monolithic reactors. A membrane can be implemented on the external surface of the monolith to obtain a monolithic membrane reactor.

The final application of a porous ceramic monolith defines the required composition, geometry, and porous structure. For example, for coatings of molecularly selective membranes, smooth monolith surfaces with small pore diameters are beneficial to achieve thin homogeneous films. For the flow to pass through the wall, a high macroporosity is advantageous, as it increases the permeability and reduces the pressure drop. For SLP applications, a high catalyst loading is essential for high conversion, and hence, a high pore volume is desired. Besides, a large specific surface area, provided by micro- and mesopores, facilitates the dispersion of the catalyst solution.

Different ceramic materials can be structured as porous monoliths [14,15]. Among them, silicon carbide (SiC) shows high values of hardness and elastic modulus, elevated phase change

temperature, thermal conductivity, and chemical inertness, making it highly promising as monolithic material [16]. Especially the high thermal conductivity of SiC alleviates problems with hot-spot formation, which are often present in catalytic beds. Porous SiC materials can readily be shaped into complex geometries at relatively low cost through an abundant number of techniques, e.g., slip casting [17–19], freeze casting [20–22], injection molding [23,24], tape casting [25,26], hot pressing [27], extrusion [18,28], and additive manufacturing [29,30]. Among the shaping techniques, extrusion allows rapid, low-cost production of SiC bodies of the desired length that can be used in various catalytic bed configurations, thereby tuning the fluid dynamic properties. The difficulty to increase the typically low specific surface area observed for porous SiC materials [31] is in stark contrast to the high values of 200-400 m^2 g^{-1} of silica and alumina supports usually applied for SLP catalysis [32], which affords an increased activity of the catalyst [33].

Recently, we have shown that the use of SiC-based monoliths for the efficient immobilization of Rh-diphosphite catalyst systems leads to very active and selective systems in the gas-phase hydroformylation of 1-butene (see Scheme 1) [34].

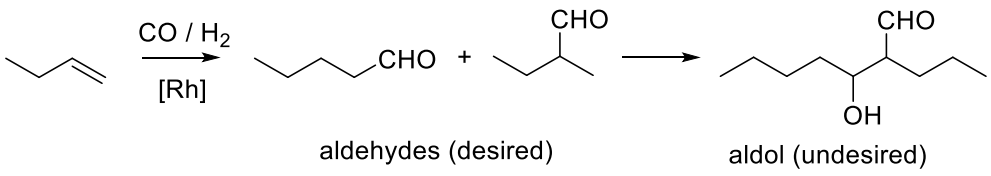

Scheme 1. Hydroformylation reaction network of 1-butene to linear (desired) and branched pentanal with an undesired consecutive aldol condensation.

This work is the first to develop a porous SiC monolith to combine the hydroformylation of 1-butene in an embedded SLP system with membrane separation. Commercial SiC extruded monoliths are tuned to obtain mechanically resistant, thermally conductive support materials that combine the benefits of cellular structures (fluid dynamics, handling, scaling-up) with the

traditional role of supports (dispersion, immobilization and shaping of active phases) and/or tailored physical or chemical properties.

2 Experimental

2.1 Preparation of SiC monoliths

SiC monoliths were manufactured by LiqTech International A/S (Figure 2) following a patented procedure [35]. A plastic formulation of α-SiC powder with well-defined particle size distribution was shaped into a multi-channel monolith by extrusion, which was then dried and sintered at an appropriate temperature. Particle sizes of 17.3 μm (fine) and 36.5 μm (coarse) were used to obtain monoliths with a finer (SiCf) or a coarser core (SiCc). A suspension of sub-micro sized α-SiC particles was subsequently applied onto the surface of the monolith body, which was then dried and sintered to form the SiC skin. For these SiC monoliths, with a hierarchical pore size distribution, an "s" was added to the name. The monoliths measured 200 mm in length, 25.4 mm in diameter, and contained 30 channels of 3 mm diameter.

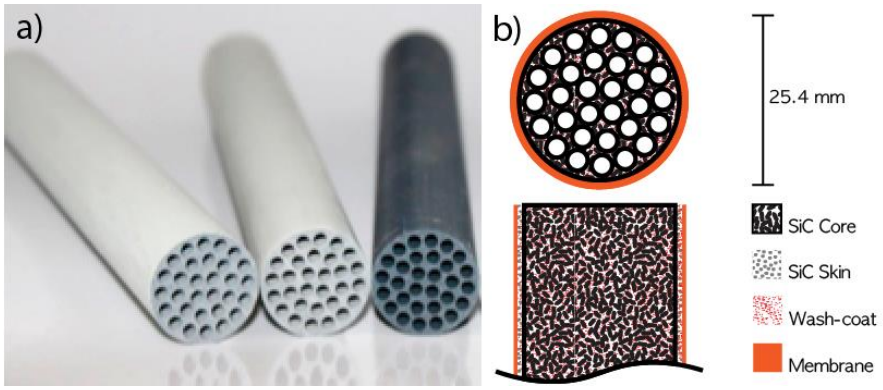

Figure 2. a) Photograph of commercial Liqtech's SiC monoliths. b) Schematic drawing of the SiC monolithic support with hierarchical porosity. The macropores of the SiC core and skin of the channeled structure can be infiltrated with metal oxide nanoparticles (silica or alumina) that form mesopores. The low-roughness skin can be coated with a non-porous molecularly selective membrane.

To generate mesoporosity and to modify the surface chemistry, the SiC monoliths were infiltrated with metal oxide nanoparticles by submerging the SiC body into a colloidal suspension followed by excess removal. Suspensions of silica with particle sizes of 7 and 70 nm and of pseudo-boehmite (an alumina precursor) with particle size distribution between 60-90 nm were used. The wash-coating process was repeated if desired until saturation was reached. The infiltrated monoliths were dried overnight, and then calcined at Ts+x (Ts = standard temperature; x between -200 and +400 ºC) with a ramp of 100 °C h^{-1} and a minimum hold time of 1 h, as disclosed in patent [36]. All chemicals were 99.8 % pure or higher and used as supplied.

2.2 Impregnation of SiC monoliths with catalyst stock solution

All syntheses and impregnation steps were carried out by standard Schlenk techniques under an argon atmosphere (99.999 %) using the chemicals as received. To prepare the catalyst stock solution, 3.76 g (4.78 mmol) of ligand (6,6′-[(3,3′-Di-tert-butyl-5,5′-dimethoxy-1,1′-biphenyl-2,2′-diyl)bis(oxy)]-bis(dibenzo[d,f][1,3,2]-dioxaphosphepin, bpp, >98 %, Evonik Oxeno GmbH) and 0.309 g (1.20 mmol) of Rh-precursor ([Rh(acac)$(CO)_2$, >98 %, Sigma-Aldrich) were each dissolved in 40 ml anhydrous CH_2Cl_2 (≥99.8 %, Sigma-Aldrich). The individual solutions were stirred for 15 min, and then mixed and stirred for 1 additional h. Afterwards, 9.20 g of bis(2,2,6,6-tetramethyl-4-piperidyl)sebacate (sebacate, >98 %, Evonik Oxeno GmbH) were dissolved in 60 ml CH_2Cl_2, stirred for 1 h, and then added to the Rh-bpp solution together with another 40 ml of anhydrous CH_2Cl_2. Following, the solution was stirred for a minimum of 2 h before further usage. By this procedure, the bpp-to-Rh molar ratio was set to 4 and the sebacate-to-Rh molar ratio to 16.

Before impregnation, the wash-coated SiC monoliths were washed in de-ionized water three times, dried in an oven at 100 °C overnight, and then placed under vacuum for a minimum of 4 h.

Impregnation was carried out by dip-coating the monoliths for a minimum of 5-6 min in the catalyst stock solution. The excess solution was drained, and the monoliths dried at room temperature with an argon flow for 24 h and subsequently under vacuum until a constant weight was obtained (typically 24 h). The amount of Rh metal in the monolith was determined by the weight increase caused by impregnation, assuming a homogeneous stock solution and total evaporation of the solvent.

2.3 Coating of SiC monoliths with a PDMS membrane

Polydimethylsiloxane (PDMS) was synthesized by reaction of a pre-polymer RTV 615 A and crosslinker RTV 615 B (Technisil) in HPLC-grade toluene (Sigma-Aldrich) as adapted from Dutczak et al. [37]. Pre-crosslinking of PDMS in toluene is advantageous because it allows tuning the solution viscosity, which makes it possible to fabricate thin and molecularly selective PDMS membranes [38].

The PDMS solution was prepared in a heat-controlled flask in which 20.45 g of RTV 615 A and 127.5 g of toluene were added and heated up to 65 °C under constant stirring of 200 rpm, where after 2.05 g of RTV 615 B was then added to start the crosslinking reaction. After about 2 h, the viscosity of the solution increased rapidly, and 150 g of toluene was added, and the stirring rate increased to 300 rpm. After reheating to 65 °C, 300 g of toluene was further added, and the stirring rate increased to 350 rpm. Once the solution started to wrap around the stirrer, the flask was placed immediately in an ice bath to quench the reaction. At this point, the PDMS synthesis was finished with a concentration of 3.75 wt.-% PDMS in toluene.

2.4 Characterization of the SiC monoliths

The textural properties were determined by mercury intrusion porosimetry (MIP) in a CE Instruments Pascal 140/240 mercury intrusion porosimeter. The samples were dried overnight at

150 ºC before analysis. The pore diameters were calculated by the Washburn equation [39], assuming a non-intersecting cylindrical pore model, using the values recommended by IUPAC for the mercury contact angle (141º) and surface tension (484 mN m^{-1}). The change from low to high pressure takes place at 30 psi, which corresponds to 7.3 µm, and may thus create artifacts at 6-8 µm. For the classification of pores, the IUPAC recommendation was followed for macro- (>50 nm), meso- (2-50 nm) and micropores (<2 nm).

High-resolution field emission scanning electron microscope (FE-SEM) images of the infiltrated monoliths were obtained on a Nova NanoSEM column microscope with Schottky filament, equipped with secondary and backscattered electron detectors. Semi-quantitative mapping was performed by energy-dispersive X-ray spectroscopy (EDX) with an EDAX Genesis XM2i detector. Monolith slices, which were cut with a precision cut-off machine (Minitom, Struers) equipped with a diamond blade, were attached to the SEM sample holder without further treatment. SEM images of the non-infiltrated monoliths were obtained on a Quanta 200 ESEM FEG operated at 15 kV. The samples were cut as described above and attached to the SEM sample holder with a copper conductive tape.

X-ray fluorescence (XRF) measurements were performed on a Bruker M4 Tornado with a Rh-X-ray-tube (measurement: 12 kV, 300 mA, spot size approximately 20 µm), Dual Si-Drift detectors (measurement: 0-10 keV), a pixel spacing of approximately 0.1 mm at a measurement time of 0.5 s $pixel^{-1}$. The samples were carefully opened with a hammer and a sharpened chisel, as this was found to be a suitable method that interfered little with the surface.

X-ray diffraction (XRD) measurements were performed with a PANalytical X'Pert Pro diffractometer using Ni-filtered Cu Kα radiation (λ = 1.5406 nm) to evaluate the effect of the calcination temperature on the crystalline structure of the metal oxide nanoparticles. XRD

analyses were performed on the colloidal suspensions (previously dried and subsequently milled) and on the infiltrated SiC monoliths.

A tabletop microscope (TM3030plus, Hitachi) was used to take high-resolution images of monoliths for evaluating the quality of the membrane coating. For sample preparation, the monoliths were placed in liquid nitrogen for 2 min, removed, and mechanical stress was applied to break them.

2.5 Gas-phase hydroformylation with catalyst impregnated SiC monoliths

The catalytic experiments were carried out in a customized set-up for continuous, gas-phase hydroformylation of alkenes [34] at a temperature of 100 °C and absolute feed pressure of 11 bar. The feed contained 1-butene (99.5 %, flow rate 0.48 mmol min^{-1}), carbon monoxide (99.97 %, flow rate 1.50 mmol min^{-1}), hydrogen (99.999 %, flow rate 1.54 mmol min^{-1}) and helium (99.997 %, flow rate 0.81 mmol min^{-1}) with the gas-flows regulated by mass-flow meters (Bronkhorst) and 1-butene dosed using a precision pump (Smartline pump 100, 10 ml pump head, Knauer). The composition of the outlet gas stream was analyzed via on-line gas chromatography (Bruker 450-GC, 2 FID, 1 TCD). The conversion of 1-butene (X) and the related turn-over-frequency (TOF, $mol_{1\text{-butene}}$ mol_{Rh}^{-1} h^{-1}) were calculated according to Equations (1) and (2).

$$\mathbf{X_{1-butene}} = \frac{\dot{\mathbf{n}}_{\mathbf{1-butene,out}}}{\dot{\mathbf{n}}_{\mathbf{1-butene,in}} - \dot{\mathbf{n}}_{\mathbf{1-butene,out}}} \quad (1)$$

$$\mathbf{TOF_{1-butene}} = \frac{\dot{\mathbf{n}}_{\mathbf{1-butene,in}} - \dot{\mathbf{n}}_{\mathbf{1-butene,out}}}{\mathbf{n_{Rh}}} \quad (2)$$

The selectivities (S) for all reaction products (i.e. n-pentanal, iso-pentanal, cis-2-butene, trans-2-butene, butane, n-pentanol, iso-pentanol, 3-hydroxy-2-propylheptanal and 2-propylhept-2-enal),

and the n/iso-aldehyde selectivity ($S_{n/iso}$) were calculated according to Equations (3) and (4), respectively.

$$\mathbf{S_i} = \frac{\dot{\mathbf{n}}_{\mathbf{i,out}}}{\dot{\mathbf{n}}_{\mathbf{1-butene,in}} - \dot{\mathbf{n}}_{\mathbf{1-butene,out}}} * \frac{\boldsymbol{\nu}_{\mathbf{1-butene}}}{\boldsymbol{\nu}_{\mathbf{i}}} \quad (3)$$

$$\mathbf{S_{n/iso}} = \frac{\dot{\mathbf{n}}_{\mathbf{n-pentanal,out}}}{\dot{\mathbf{n}}_{\mathbf{n-pentanal,out}} + \dot{\mathbf{n}}_{\mathbf{iso-pentanal,out}}} \quad (4)$$

2.6 Membrane permeation experiments using SiC monoliths

Pure-gas membrane permeation experiments were performed in dead-end mode with N_2 and CO_2 test gases (≥99.99 %, Westfalen AG) by placing the membrane-coated SiC in an oven at a temperature ranging from 20 to 120 °C. Gas permeances (see ESI for details) were measured at constant pressure with a variable volume set-up. The SiC monoliths were one inch (2.54 cm) in diameter with an active membrane length of 15.5 cm, which resulted in a membrane area of 123.7 cm². The membrane-coated SiC monolith was installed in a stainless-steel module and sealed with temperature resistant fluoroelastomer (FKM) o-rings (Landefeld), as shown in picture SI1 in the SI. Feed pressures were set to 3 and 7 bar, respectively, while the permeate pressure was at atmospheric pressure. The permeate flux through the membrane was measured with a manual bubble flow meter. Each measuring point was kept at a steady state for at least 15 min.

3 Results and Discussion

The textural properties of commercial SiC monoliths were modified to meet the requirements of a wide range of applications, more precisely to be used in catalytic membrane reactors, and specifically with supported liquid phase catalytic systems, leading to highly intensified processes. Gas-phase hydroformylation with in-situ product removal through a molecularly selective membrane was selected as case study to evaluate the feasibility of using the modified monoliths as support for the SLP catalyst and the polymeric membrane.

3.1 Design of SiC monoliths with hierarchical porosity

3.1.1 SiC core

As-prepared SiC core monoliths have a macroporous structure with a monomodal size distribution and a total pore volume of 0.2 ml g^{-1}, as determined by MIP. Figure 3 compares the size of the macropores obtained using either the fine (17.3 µm) or the coarse (36.5 µm) SiC particles as starting material to produce the core of the monolithic support in SiCf and SiCc, respectively. Samples based on the former starting material exhibited a pore distribution around 7.5 µm, while the monoliths based on the latter exhibited pores around 14.9 µm.

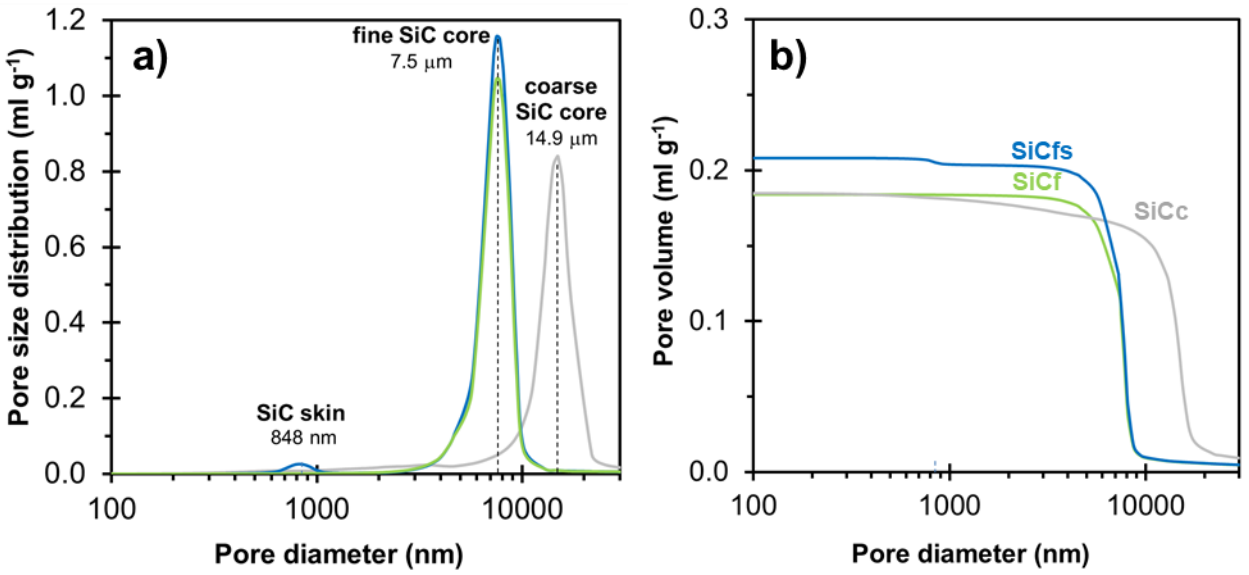

Figure 3. Results of mercury intrusion porosimetry for the coarse SiC monolith (SiCc, grey), and the fine SiC monolith without (SiCf, green) and with (SiCfs, blue) the SiC skin. a) dV/DlogD, b) Cumulative pore volume.

These pore size distributions are in good agreement with the rule of thumb that the diameter of the interstitial pores is about 40 % of the diameter of the particles that generate the voids [40]. Thus, the size of the macropores of the SiC core was tailored by the adequate selection of the particle size of the starting material.

3.1.2 SiC skin

When the selected SiC core was dip-coated into a suspension of SiC particles with a few microns in size, the external surface roughness reduced without altering the composition of the support. Figure 3 suggests that the addition of a thin SiC skin using powders of much smaller particle size than the core did not significantly alter the core porosity, but generated smaller macropores of 848 nm on the external surface. Figure 4 shows SEM images of the core and the skin. Figure 4a) shows the morphology of the SiC core, with large macrovoids between SiC particles of a smooth surface. A few micrometer-sized particles looking like residuals were also observed, which most likely originated from the sample cutting, inhomogeneity of the initial SiC powder, or infiltrated particles that reached the core during the formation of the SiC skin by impregnation. Figure 4b) depicts the defect-free SiC skin, of which the thickness was determined to be around 45-60 µm. A well-defined bimodal distribution of macropore sizes was found for the sample with the SiC skin, combined with a smooth surface, while the total pore volume was kept substantially unchanged.

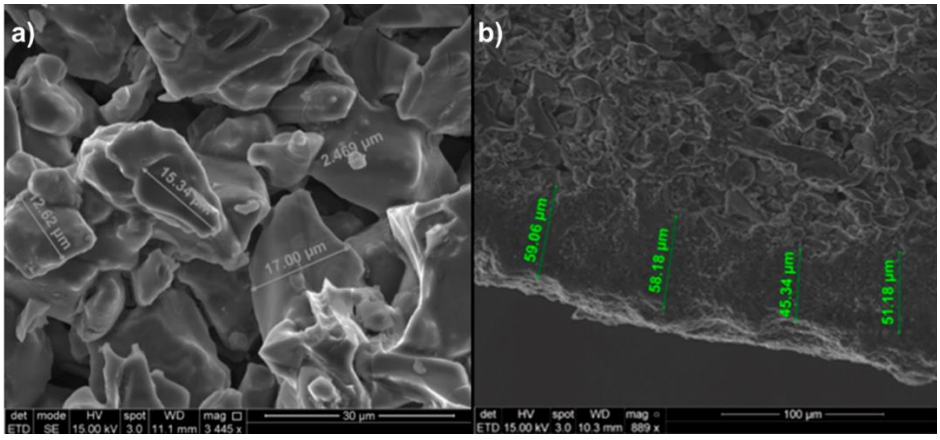

Figure 4: SEM images of SiCfs monolith with a focus on the SiC core (left) and on the SiC skin (right).

3.1.3 Infiltration of oxide nanoparticles

Subsequent immersions of the SiCfs monolith into colloidal suspensions of silica (two different particle diameters, 7 or 70 nm) or hydrated alumina (diameter in the range of 60-90 nm) resulted

in a linear weight gain until full saturation of the pores (see Figure SI2). Saturation occurred after three immersions in the alumina solution, four immersions in the small silica particle suspensions, and two immersions in the solution with larger silica particles. In the latter case, the weight-gain further increased with three and four wash-coats, but the silica accumulated on the external wall instead of infiltrating the monolith. Therefore, the maximum weight gain using silica particles of 7 and 70 nm were 17 and 20 %, respectively. Meanwhile, the maximum weight gain with alumina particles was only 14 %. The infiltration of the SiC monolith with metal oxide nanoparticles was successful in tuning the physicochemical properties of the starting material.

The following two sections present two design examples. In the first one, the objective was to modify the surface chemistry of the SiC monoliths to fit the requirements of the SLP hydroformylation catalyst. In the second one, the aim was to modify the porous structure to reduce the pore size and increase the pore area for improved catalyst impregnation.

a) To slightly tune the chemical properties without significantly altering the porosity of the monolithic structure, metal oxide nanoparticles deposition was performed by a single immersion into the colloidal solutions, followed by calcination at Ts+400 ºC (>1000 ºC). Figure 5 shows the pore size distribution obtained with SiCfs infiltrated by this procedure with silica and alumina. The macroporosity was substantially similar to that of the non-infiltrated monoliths; however, in the case of the alumina wash-coat, the macropores entrance appeared to be somewhat covered by the oxide, as the size was reduced to 5.7 µm, although the volume remained roughly the same (0.19 ml g^{-1} in the infiltrated vs. 0.21 ml g^{-1} in the non-infiltrated). Besides, smaller macropores and micropores of around 15 nm were created in very low amounts. XRF mapping revealed the even distribution of the wash-coated metal oxide inside the monolith (see Figure SI3).

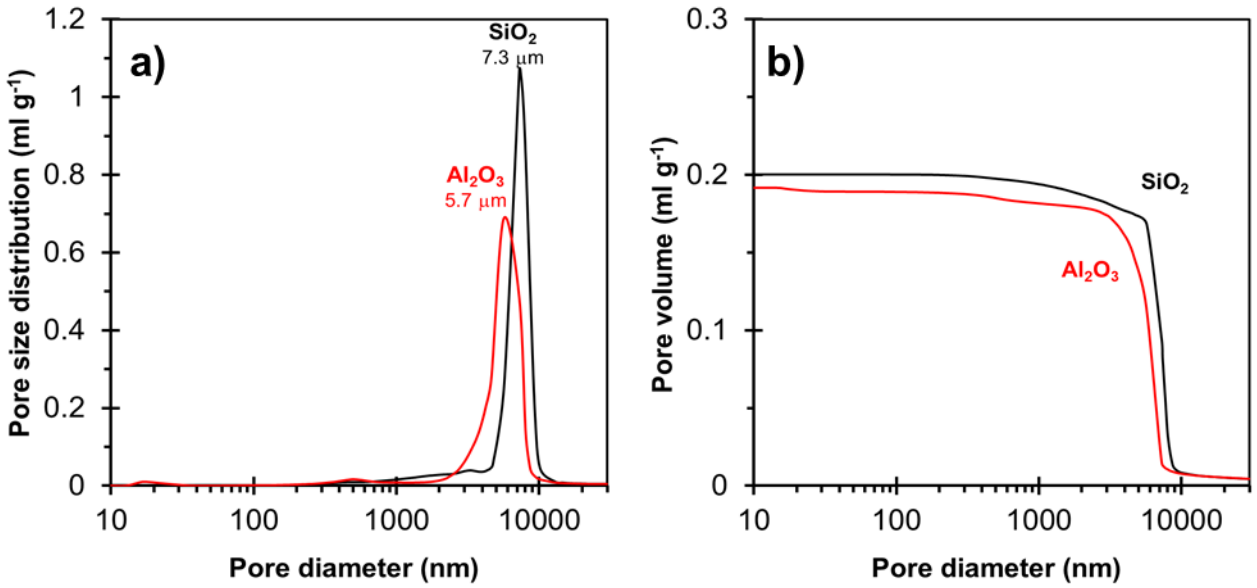

Figure 5. Porous distribution (a) and cumulated pore volume (b) of the SiCfs monoliths infiltrated once by wash-coat with either 7 nm colloidal silica particles (1xSi7, black) or 60-90 nm colloidal alumina particles (1xAl, red) and calcined subsequently at Ts+400 ºC.

b) To obtain a new porous distribution, multiple wash-coats were applied to the SiC structure, to incorporate a larger amount of metal oxide nanoparticles. Besides, the calcination was performed at moderate temperatures (below 1000 ºC) to avoid the sintering of the oxide. The interstitial voids among the SiC macroparticles were filled, at least partially, with metal oxide particles, which led to the formation of two kinds of smaller pores. Thus, the monoliths infiltrated by this procedure presented a trimodal pore-size distribution, with some remaining big macropores, new smaller macropores, and mesopores. The origin of the smaller macropores can be attributed to an accumulation of the metal oxide onto some of the macropore walls, causing a reduction of the neck size. The size and volume of these pores increased with the calcination temperature due to the stronger contraction suffered by the metal oxide particles treated at a higher temperature. The mesopores are the voids between the nanoparticles. In the case of silica, these are expected to be stable at the calcination temperatures employed. The accumulated pore volume and pore size distributions obtained at maximum silica loadings are depicted in Figure 6, while Table SI1

summarizes the pore volume fraction for each kind of pore. According to the rule of thumb of 40 %, as mentioned above, the size of the silica nanoparticles estimated from the size of the mesopores agrees well with the specifications of the colloidal solutions. The voids generated with the small (7 nm) and the larger (70 nm) nanoparticles were around 5 and 24 nm in diameter, respectively (see the comparison in Figure SI4). The presence of the thin SiC skin had no clear effect on the porosity induced by the infiltration process; the MIP results were similar. At lower metal oxide loadings, the volume of the new meso- and macropores was smaller (see Figure SI5 for 70 nm silica wash-coat), and the volume of the macropores between the SiC particles larger, as the latter were only partially filled.

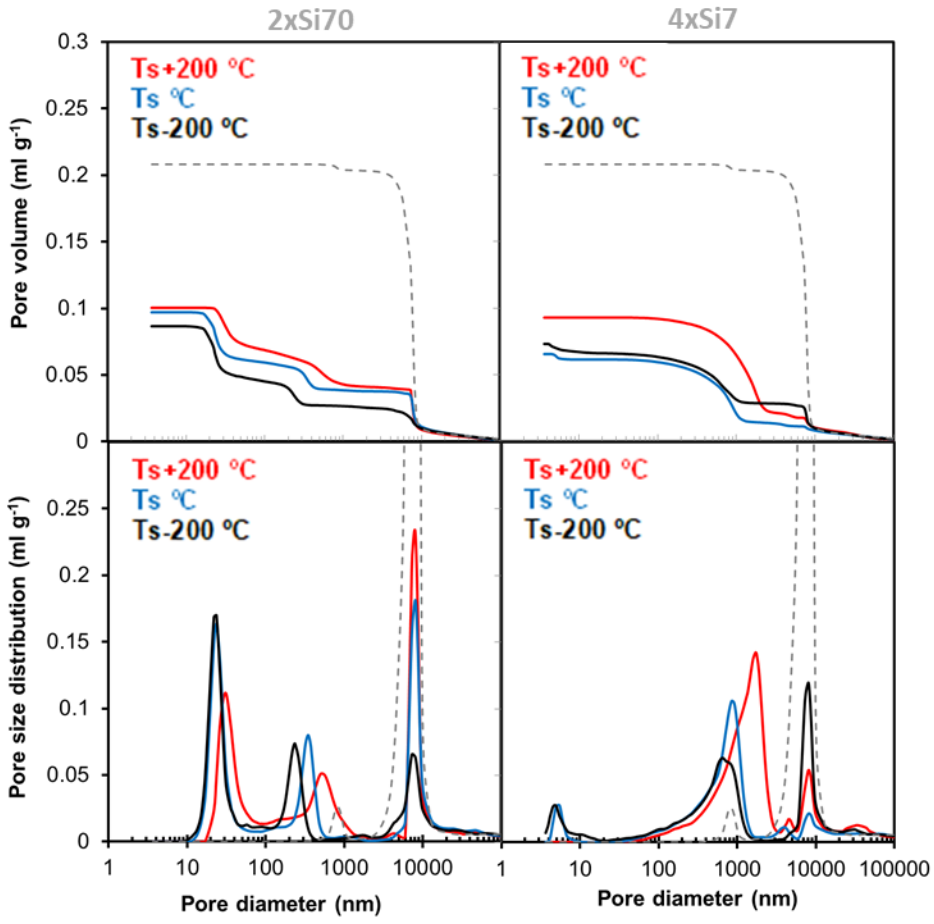

Figure 6. Accumulated pore volume (top) and pore size distribution (dV/dlogD, bottom) of the SiCfs monolith infiltrated with silica and calcined at different temperatures. The curves of the

non-infiltrated monolith are included as a reference (dashed line). Left: Two immersions in the colloidal solution with 70 nm particles (2xSi70). Right: Four immersions in the 7 nm colloidal solution (4xSi7).

Figure SI6 compares the porosity of as-synthetized and 2xSi70 infiltrated SiCfs and SiCcs monoliths. The mesopores were similar in both wash-coated SiCfs and SiCcs samples, as they mainly depended on the metal oxide particle packing. The size of the larger pores in the infiltrated SiCcs was reduced by a factor of two, as can be seen from comparing the region of small macropores. This observation agrees well with the assumption that the neck size reduced by the accumulation of the metal oxide nanoparticles on the walls of the large macropores. Moreover, this shift corroborated that the small macropores were not associated with cracks in the silica wash-coat generated during drying or calcination. In addition, the interstitial voids of the SiCcs sample were not filled completely, indicating that higher loading was required to fill these larger pores.

In the case of infiltration with alumina, the pore size distribution obtained at maximum loading was rather unaffected by the calcination temperature in the applied range (Figure SI7). The alumina nanoparticles are expected to be 25-30 nm in diameter when taking into account the diameter of the mesopores generated in the calcined alumina-infiltrated monolith. This size is three times smaller than the 60-90 nm reported for the aluminum hydroxide precursor in the specifications of the colloidal solution used for the wash-coat. On the one hand, this effect could be caused by the transformation of the hydrated precursor into the oxide during the calcination step, which may reduce the particle size, and, consequently, the void between them; this dehydration produced in the alumina-wash-coated samples also explains the lower weight gain and larger size of generated small macropores compared to the monoliths infiltrated with silica. On the other hand, the broad particle size distribution of the alumina nanoparticles led to a closer packing, decreasing the pore size compared to that obtained with particles of very similar sizes

[41]. EDX mapping of the core and skin of 4xAl-Ts SiC monolith show the homogenous distribution of the wash-coat (Figure SI9). It is also noteworthy that the pore volume of the monoliths infiltrated with alumina was similar to that of the non-infiltrated sample, suggesting that the saturation was not reached due to complete pore filling, but by pore entrance blocking after the first wash-coats.

The specific surface area determined by MIP of 0.1 $m^2 g^{-1}$ for the non-infiltrated monoliths (SiCfs) was rather low. In contrast, the infiltrated samples calcined at moderate temperatures presented significantly higher values, as specific surface area essentially depends on the size and volume of micro- and mesopores. Figure SI8,b) depicts the specific surface area as a function of the colloidal solution employed for the wash-coat and the calcination temperature. The highest value was obtained for the sample infiltrated with alumina four times, due to the higher volume of relatively smaller mesopores (see Figure SI7).

As the mesopores are voids between the nanoparticles, they were somewhat independent of the calcination temperature. However, size changes in the mesoporous region at the highest calcination temperature of Ts+400 ºC suggest some particle sintering, leading, in the case of the 70 nm silica wash-coat, to the formation of larger agglomerates and, therefore, larger voids in-between. In the case of the 7 nm particles, the interparticular voids disappeared (see Figure 6), indicating a complete elimination of the particular structure. The mobility temperature of solid metal oxides (when the particles start to move and rearrange) or the Tammann temperature (the minimum temperature at which a solid would undergo a solid-solid interaction) are around half of the bulk melting point in K [42], and explain these effects. At this temperature, i.e. ca. 900 ºC for Al_2O_3 and 700 ºC for SiO_2 [43,44], the diffusion of ions and cavities are activated and, consequently, grain boundary integration and formation of agglomerates becomes relevant. Thus, the sintering process occurs much below the melting point of the nanoparticles. Moreover, the

Tammann temperature decreases as the size of the particles decreases. The FE-SEM images in Figure 7 confirm these findings. Micrographs of silica-infiltrated samples calcined at Ts are shown in Figures 12a and 12c. The images revealed spherical silica particles on the surface of the SiC core and the small macropores detected by MIP. As the effect of sintering was more severe for the 7 nm silica wash-coat, at Ts+200 ºC the 7 nm particles could not be detected and the mesoporosity disappeared (see Figure 7,d), while the morphology of the 70 nm particles was essentially maintained (see Figure7,b), so the mesoporosity was still present in the samples infiltrated with 70 nm silica particles at this temperature. The same was observed at lower silica loadings by MIP and microscopy (results not shown).

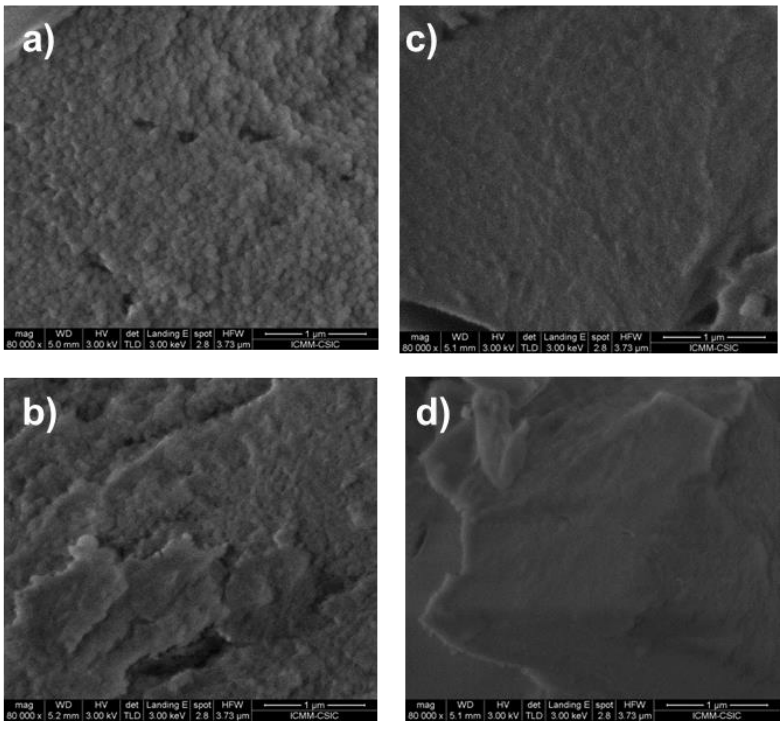

Figure 7. FE-SEM images of silica-infiltrated SiCfs. a) Two immersions in 70 nm silica, calcination at Ts ºC (2xSi70-Ts); b) Two immersions in 70 nm silica, calcination at Ts+200 °C (2xSi70-Ts+200); c) Four immersions in 7 nm silica, calcination at Ts ºC (4xSi7-Ts); d) Four immersions in 7 nm silica, calcination at Ts+200 °C (4xSi7-Ts+200).

Additional information about the effect of the calcination temperature on the infiltrated oxide nanoparticles can be extracted from the analysis of their crystalline structure. The XRD patterns in Figure 8,a were acquired with the powders obtained by drying and calcining the colloidal solution of 70 nm silica. The absence of sharp peaks indicates that the silica calcined at Ts-100 ºC was mostly amorphous, whereas at Ts+400 ºC a sharp diffraction peak appeared at $2\theta = 22^{o}$, corresponding to the cristobalite crystalline phase of silica (PDF card number 01-076-0939) with a minor contribution of the tridymite phase (PDF card number 01-077-0126). The diffraction patterns of the calcined SiCfs monolith infiltrated twice with the solution (2x70Si) contained, besides characteristic SiC diffraction peaks (not shown), a characteristic diffraction peak indicating the presence of the cristobalite phase (Figure 8,b), and the size of the silica crystalline domains was slightly more apparent at higher loadings (compare 1x70Si-Ts+200 and 2x70Si-Ts+200). No significant differences were observed in the diffractograms between calcination at Ts or Ts+200 ºC, but at Ts+400 ºC silica crystallization was strongly promoted, resulting in more intense cristobalite peaks along with the formation of the tridymite phase. Hence, the XRD results confirmed that the destruction of the nanoparticular structure at high calcination temperatures was accompanied by the growth of crystalline domains, which may be relevant for the catalytic activity of the supported catalyst.

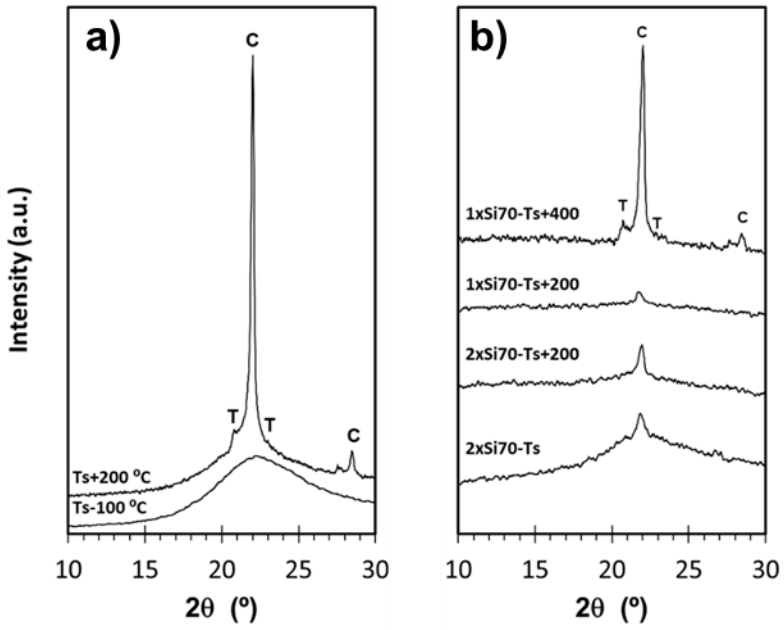

Figure 8. XRD patterns of a) the calcined colloidal solution of 70 nm silica, and b) the SiCfs monolith infiltrated with this solution. T = tridymite, C = cristobalite.

3.2 Gas-phase hydroformylation using tailored catalytic SiC monolith

The wash-coated SiC monoliths with hierarchical porosity are a suitable structured support material for an active and selective liquid-phase catalyst system. Accordingly, a SiCfs monolith infiltrated with silica (1x7Si-Ts+400) was impregnated with an active Rh-bpp-sebacate catalyst system and tested in the hydroformylation of 1-butene (Rh-loading = 11.97 mg). The conversion and TOF of 1-butene, as well as reaction selectivities, are shown in Figure 9 with combined isomerization selectivity for cis-2-butene and trans-2-butene and aldol selectivity for 3-hydroxy-2-propylheptanal and 2-propylhept-2-enal. The butane selectivity remained constant at 1 %, and alcohols were not detected at all. Therefore, these data are not included.

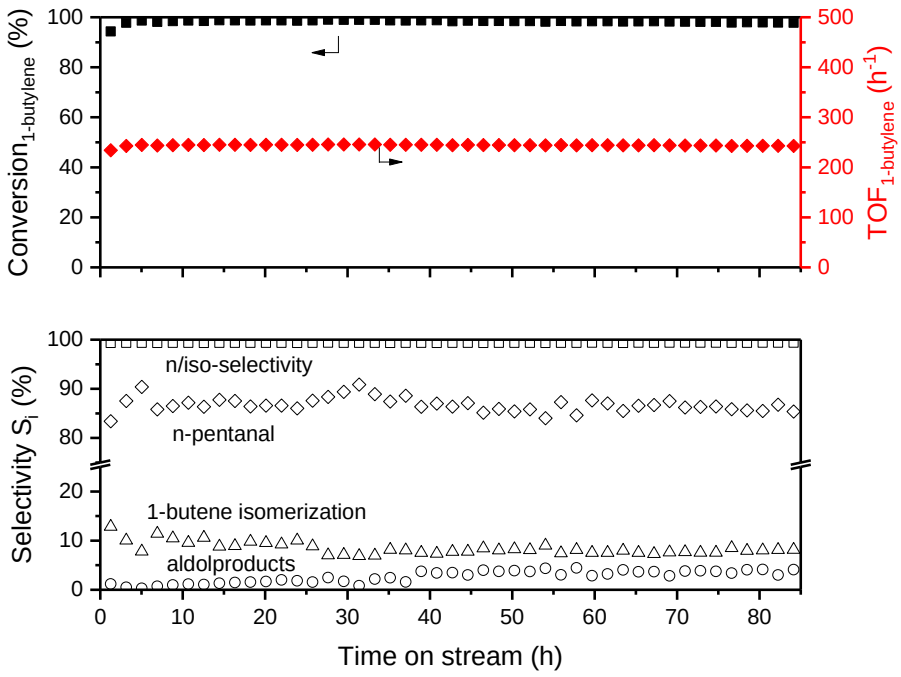

Figure 9. Catalytic testing in the hydroformylation reaction of 1-butene with 1x7Si-Ts+400 SiCfs monolith impregnated Rh-bpp-sebacate catalyst system. No external membrane coating applied. Reaction conditions T = 100 °C, p_{feed} = 11 bar, $\dot{n}_{H2,feed}$ = 1.54 mmol min^{-1}, $\dot{n}_{CO,feed}$ = 1.50 mmol min^{-1}, $\dot{n}_{He,feed}$ = 0.81 mol min^{-1}, $\dot{n}_{1\text{-butene,feed}}$ = 0.48 mol min^{-1}, bpp/Rh mol ratio = 4, Rh-loading = 11.97 mg.

As seen in Figure 9 (top), almost full conversion of 1-butene was achieved (relates to an average catalyst TOF of 245 h^{-1}), with essentially no deactivation (< 1 %) during the examined 85 h time on stream. High selectivity of 86 % towards the desired n-pentanal product and >99 % n/iso-aldehyde selectivity was achieved at steady-state, which are comparable to previous reports using bpp as the ligand [41]. The high n/iso-ratio confirmed that the catalytically active Rh-bpp catalyst remained intact as ligand dissociation would have lowered the n/iso ratio significantly as generally found for hydroformylation catalysts [8]. Despite the high amount of n-pentanal formed in the reactor, the selectivity for the consecutive reaction to form undesired aldol products occurred only to a minor extent, with 3.5 % average selectivity during steady state. In addition, the selectivity of 7.8 % for 1-butene isomerization was relatively low. Overall, the investigated

support shows exciting results for an application in the continuous gas-phase hydroformylation of 1-butene.

3.3 Polymeric membrane coating on the exterior surface of SiC monolith

To show the applicability of a gas separating membrane on this ceramic support material, a thin and molecularly selective polydimethylsiloxane (PDMS) membrane was coated on a SiC monolith. The macropores on the external surface of both SiCf and SiCc monoliths were prone to pore intrusion, which prohibited a defect-free PDMS layer from being formed. However, PDMS was successfully dip-coated onto the SiCfs monoliths, which have smaller pores on the external surface. In a first approach, a three-layer coated PDMS membrane with a thickness of around 100 µm was successfully formed onto the SiCfs monolith. The layer number was consecutively decreased to a double-layer-coating or even a single-layer-coating, thus reducing the membrane thickness. Figure 10 shows a double-coated and a single-coated PDMS membrane on the SiCfs monolith, prepared with an insertion speed of 10 mm s^{-1}, a holding time of 60 s, and a withdrawal speed of 10 mm s^{-1}. The average thickness was 27 and 13 µm, respectively.

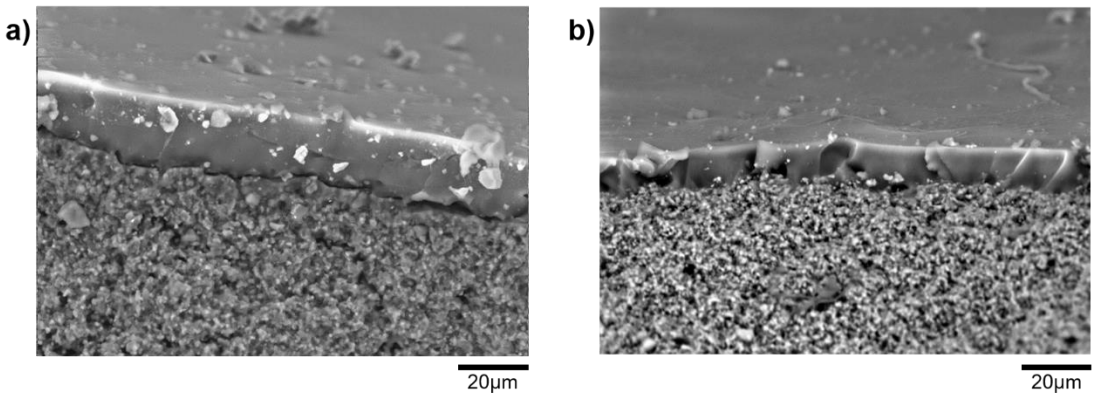

Figure 10. PDMS membrane on SiCfs monolith with an insertion speed of 10 mm s^{-1}, a holding time of 60 s, and a withdrawal speed of 10 mm s^{-1}. a) Double-coated PDMS membrane, b) Single-coated PDMS membrane.

The results of CO_2 and N_2 permeation experiments on the SiCfs monoliths shown in Figure 11 gave a CO_2 to N_2 selectivity >10 for each tested membrane at room temperature, in line with the range of selectivity values reported in literature [45,46] and agree with the PDMS membrane thicknesses observed by SEM. The influence of the withdrawal speed from the PDMS solution was also analyzed and indicated that a faster withdrawal speed led to a decrease in permeance, i.e., an increase in layer thickness. This phenomenon follows the Landau-Levich model, which states that above a minimal velocity the influence of solution adhesion compared to gravity becomes prominent, and thus more solution sticks to the surface with higher velocity [47].

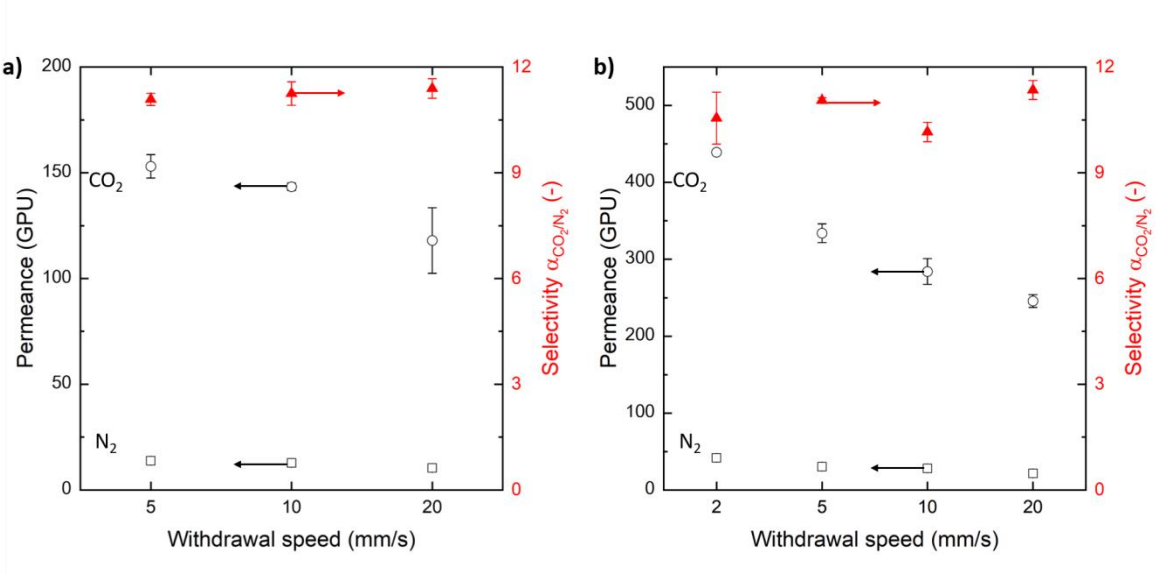

Figure 11. Permeance and CO_2/N_2 selectivity over withdrawal speed of a) double-coated PDMS membrane on SiCfs monolith b) single-coated PDMS membrane on SiCfs monolith. Constant insertion speed of 10 mm s^{-1}, holding time of 60 s. The permeance measurements were performed at 22 °C and with a feed pressure of 3 bar against 1 bar permeate pressure.

Mechanical stability and temperature resistance were also examined for SiCfs monoliths with triple- and single-coated PDMS membranes, respectively (Figure 12). Both membranes were found stable at temperatures of 120 °C and feed pressures up to 7 bar, with a trans-membrane pressure difference of 6 bar. Furthermore, both achieved expected selectivities for CO_2/N_2,

confirming that the membranes were defect-free. However, the single-coated membrane displayed almost seven-fold higher permeances compared to the triple-coated membrane, which is in good agreement with the difference in thickness and shows the benefit of the coating-layer reduction.

The CO_2/N_2 selectivity of the membranes declined with increasing temperature, which is due to the evolution of the sorption and diffusion coefficients of the individual gas molecules in PDMS with increasing temperatures. On the one hand, the CO_2 sorption coefficient decreases for elevated temperatures, whereas the sorption coefficient of N_2 increases in polymeric rubbery membranes if the temperature rises [48]. On the other hand, the diffusion coefficients of both gases increase, which combined led to an overall decrease of the CO_2/N_2 selectivity at high temperatures.

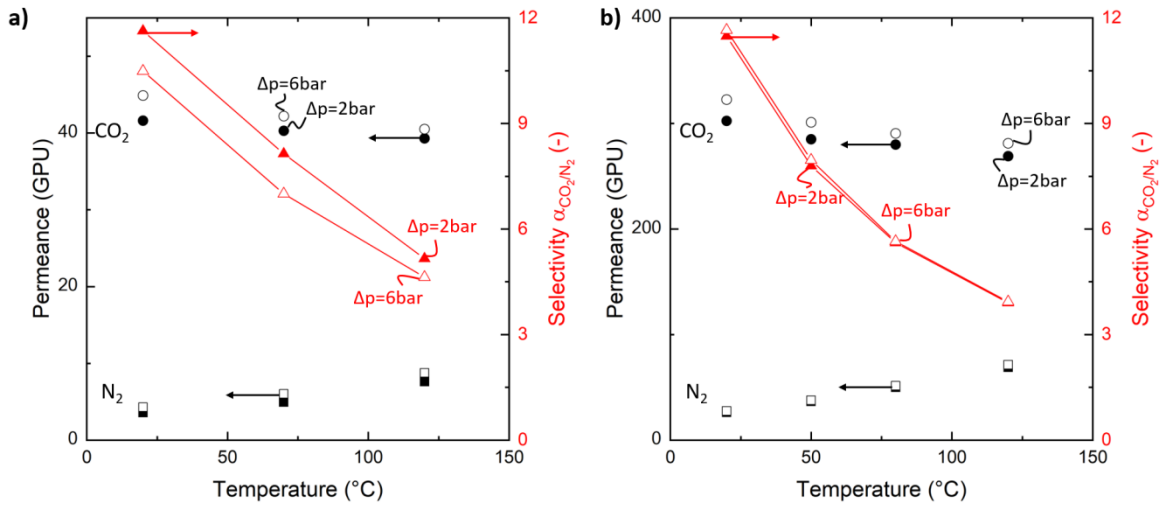

Figure 12. Permeance and CO_2/N_2 selectivity over temperature for a) triple-coated PDMS membrane on a SiCfs monolith, b) single-coated PDMS membrane on a SiCfs monolith. Insertion speed of 10 mm s^{-1}, holding time of 60 s, withdrawal speed of 10 mm s^{-1}. The transmembrane pressure was set to Δp=2 bar with a feed pressure of 3 bar (see filled symbols) and Δp=6 bar with a feed pressure of 7 bar (see empty symbols). In both settings, the permeate pressure was at 1 bar.

4 Conclusions

Suitable monolithic supports for SLP catalysis in membrane reactors were developed. Wall-flow, multi-channeled SiC monoliths with macro-voids of a specific diameter were obtained by extrusion and various post-treatments allowed further tuning of properties that can be selected according to the design requirements of the final application of the supports.

SiC monoliths with hierarchical bimodal porous distributions were obtained by forming a perfect skin on the external wall without altering the internal porosity of the structure. The smooth surface of this skin was successfully coated with a defect-free, thin, and molecularly selective PDMS membrane, which was permeable and stable up to temperatures of 120 °C and feed pressures of 7 bar, with a transmembrane pressure of 6 bar. The membrane-coated macroporous SiC monolith may be utilized in gas- or liquid-separation applications, as, for example, in a membrane reactor for a process like the described 1-butene hydroformylation reaction.

Immersion of the SiC monoliths into colloidal solutions of silica or alumina particles followed by calcination provided SiC structures with a homogeneously infiltrated metal oxide support on the exposed surface. The porosity was not significantly altered at low loading and calcination temperatures higher that the Tammann temperature. On the contrary, the textural properties were modified by applying multiple wash-coats and calcination at moderate temperatures, to avoid sintering effects. Both silica or alumina wash-coating procedures resulted in trimodal porous distributions with unfilled large macropores, smaller macropores created by the accumulation of the oxide on some of the macropore walls, and mesopores formed by the voids between the nanoparticles. The size of the new meso- and macropores were tunable by selection of the SiC and oxide particles, resulting in mesopore diameters of 5 and 24 nm when infiltrating 7 and 70 nm silica particles, respectively, in the SiC structure with pores of 7.5 µm, whereas the mesopores of the alumina infiltrated monolith were 10 nm in size. The size and volume of the small macropores generated by the deposition of silica nanoparticles increased with the

calcination temperature. Meanwhile, higher silica loadings reduced the volume of the big macropores between the SiC particles as they were increasingly filled, while the volume of the new meso- and macropores increased concurrently.

The silica-infiltrated SiC monolith was utilized to efficiently immobilize a liquid-phase catalyst system containing dissolved Rh-bpp complexes (i.e., monolithic SLP system). The catalytic performance of the resultant monolith impregnated with the liquid film containing the catalyst system was demonstrated in long-term operation for continuous gas-phase 1-butene hydroformylation, maintaining >98 % conversion over 85 h time on stream with high selectivity toward the desired linear aldehyde.

The structures developed in this work allowed the successful application of SiC monoliths wash-coated with silica and coated with a PDMS membrane as support for SLP Rh-bpp-sebacate catalysts in catalytic membrane reactors for the hydroformylation of 1-butene [34]. The desired n-aldehyde can be accumulated over the substrate 1-butene by a factor of 2.2. While this value is probably too low for industrial application, it shows the high potential of the studied monolithic SLP catalysts for process intensification, where the aldehyde product is partially removed from the reactor to circumvent consecutive aldol byproduct formation. Overall, this study shows the feasibility of using SiC monoliths for the design of catalytic membrane reactors. The creation of mesopores provides surface area for better catalyst dispersion and small pore sizes that allow better immobilization of liquids by capillary forces. Multiple potential applications using monolithic SLP systems are anticipated, e.g., for supported ionic liquid phases (SILP), with negligible vapor pressure of the applied solvent, in exothermic and endothermic equilibrium reactions with in-situ removal of one of the products to shift the equilibrium.

5 Acknowledgements

The authors gratefully acknowledge financial support from the European Commission within the Horizon2020-SPIRE project ROMEO (Grant Agreement Number 680395). Furthermore, the authors would like to thank Dr. Andreas Bösmann and M. Sc. Patrick Wolf (Universität Erlangen-Nürnberg) for the XRF measurements, as well as Markus Wist (RWTH Aachen University) for his work in the membrane fabrication.

6 Supporting information

6.1 Gas transport through molecularly selective polymeric membranes

Gas transport through dense polymer films is based on the solution-diffusion mechanism. The solution-diffusion mechanism consists of three steps, which are the sorption of molecules into the membrane surface at the high-pressure side, molecule diffusion through the membrane, and molecule desorption from the membrane surface at the low-pressure side. These three steps govern the time it takes for a molecule to move from the high-pressure feed side to the low pressure permeate side is expressed in the material-specific permeability P [48,49]:

$$P = S * D \quad \text{(S1)}$$

Here, S is the sorption coefficient, and D is the diffusion coefficient. The unit of permeability is Barrer [1 Barrer = $1 \cdot 10^{-10}$ cm^3(STP) cm cm^{-2} s^{-1} $cmHg^{-1}$]. When P is determined experimentally, it is often calculated by Equation (S2).

$$P = \frac{\dot{V}(STP) * \delta_{mem}}{A_{mem} * (\Delta p)} \quad \text{(S2)}$$

$\dot{V}(STP)$ is the flux through the membrane at standard conditions, A_{mem} is the active membrane area, δ_{mem} is the membrane thickness, and Δp is the pressure difference from feed to permeate

side. If the membrane thickness is unknown or difficult to determine, the membrane-specific permeance Q can be measured instead of the permeability [50].

$$Q = \frac{P}{\delta_{mem}} \quad \text{(S3)}$$

The unit of permeance is expressed in GPU [1 GPU = $1 \cdot 10^{-6}$ cm^3(STP) cm^{-2} s^{-1} $cmHg^{-1}$]. With the single-gas permeance data of two components, an ideal selectivity for component i and j is calculated according to Equation (S4).

$$\alpha_{i,j} = \frac{P_i}{P_j} = \frac{Q_i}{Q_j} \quad \text{(S4)}$$

6.1 Figures

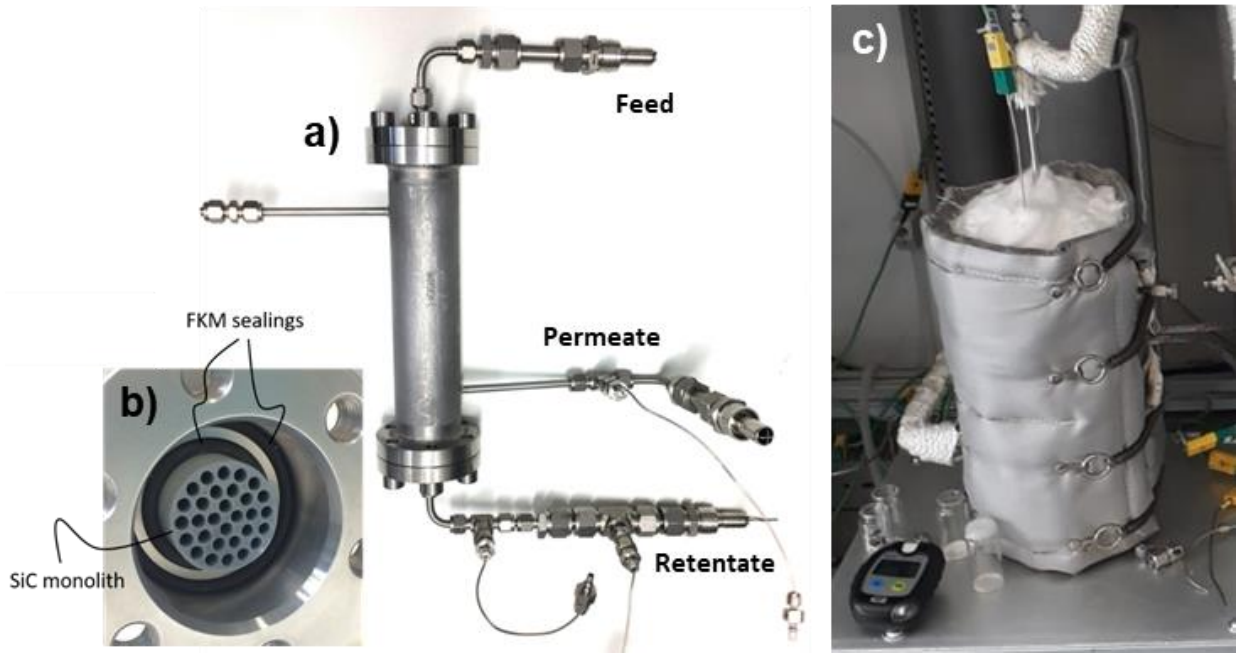

Figure SI1: a) Stainless steel module with quick couplings for easy installation into permeation/reaction measurement set-up, b) Monolith sealed with FKM o-rings in the module, c) Module assembled with heating jacket for catalytic experiments.

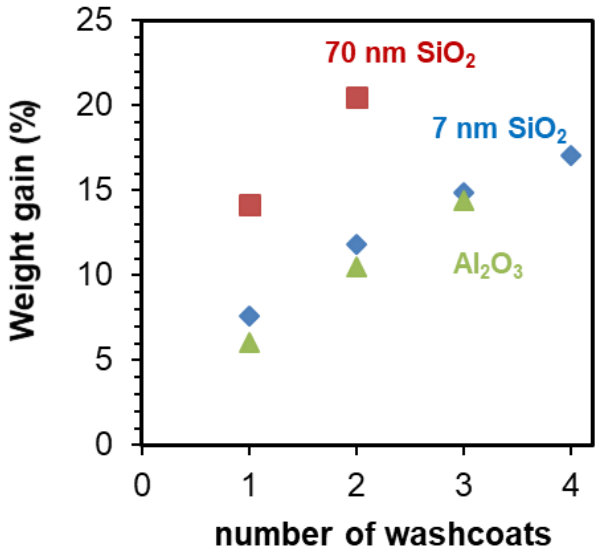

Figure SI2. Weight gained by incorporation of metal oxide nanoparticles into the SiCfs monolith as a function of the number of immersions into colloidal solutions with alumina or silica with two different particle sizes. The wash-coating weight was defined by the mass of the uptake of dry wash-coat over the initial mass of the specimen.

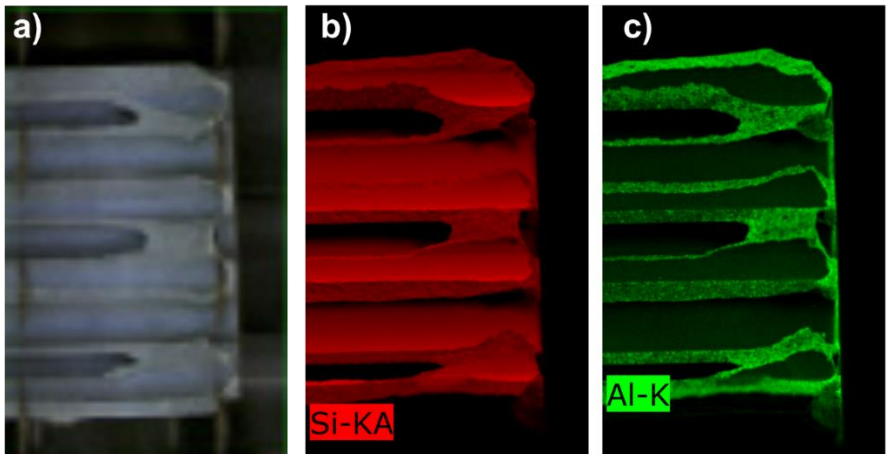

Figure SI3. a) Overview image of a SiCfs monolith infiltrated with Al_2O_3 and calcined at Ts+400 °C opened longitudinally for XRF analysis (image size: 6000x2901 px). Silicon (b) and aluminum (c) XRF mappings on the monolith (image size: 202x323 px, mag: 0x, HV: 12.0 kV, puls th.: 27.41 kcps.

The distribution of the wash-coated metal oxide inside the monolith was analyzed by XRF. Figure SI3 shows an overview image of the SiCfs $1xAl_2O_3$ specimen calcined at Ts+400 ºC and

longitudinally opened for analysis. The sample was scanned for aluminum as an indicator for the infiltrated Al_2O_3 and silicon as an indicator for SiC. As expected, the Si scan showed an even distribution with some areas of lower intensity around sharp edges, while the scan for Al exhibited a full distribution of the Al_2O_3 wash-coat over the specimen. As a result of the focal depth the lowest intensity was found on the channel walls, as the channels have a diameter of 3 mm. The wash-coat seemed evenly distributed throughout all sites of fracture, indicating that the wash-coat penetrated the pore structure of SiC. Notably, the intensity of the Al signal in the outer wall (top and bottom of the monolith in Figure SI3) was somewhat higher than in the internal walls of the monolith. This indicates that penetration of the aluminum colloidal solution during the wash-coating procedure was hampered before all the pores were filled. Similar observations also applied for the center and left parts of the specimen. Several parameters can be optimized, such as the size of the particles, the viscosity of the solution, or the number of wash-coats to avoid alumina accumulation on the external wall.

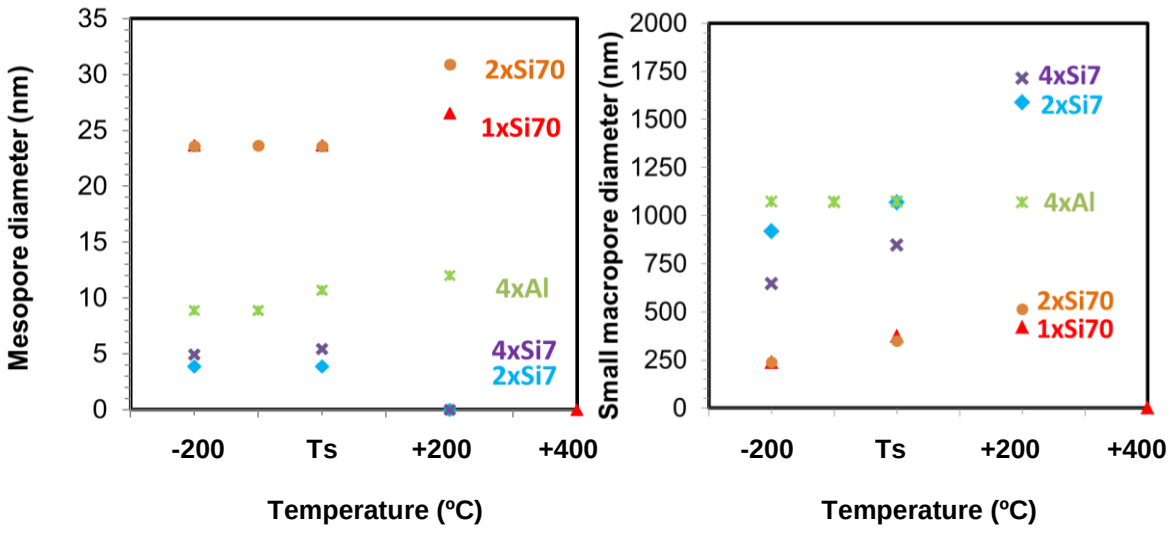

Figure SI4. Porosity created in the SiCfs monolith by infiltration with the different colloidal metal oxide solutions as a function of the calcination temperature. Left: Size of the pores created by the oxide interparticular voids. Right: Size of the small macropores created by neck size reduction.

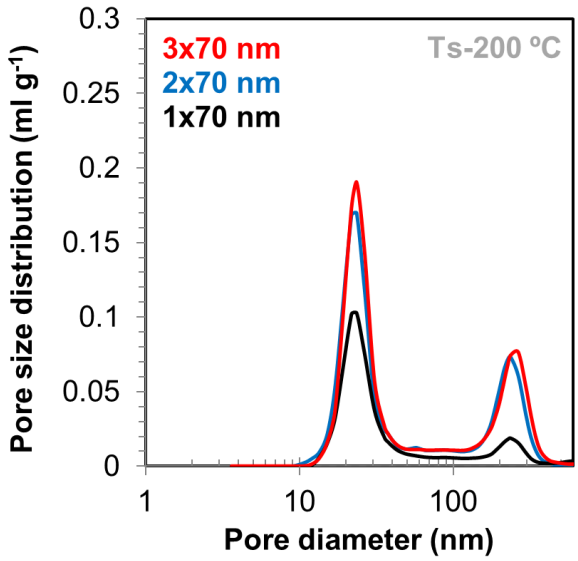

Figure SI5. Effect of the number of wash-coats on the pore size distribution of SiCfs monoliths infiltrated with colloidal silica nanoparticles of 70 nm. Calcination temperature: Ts-200 ºC.

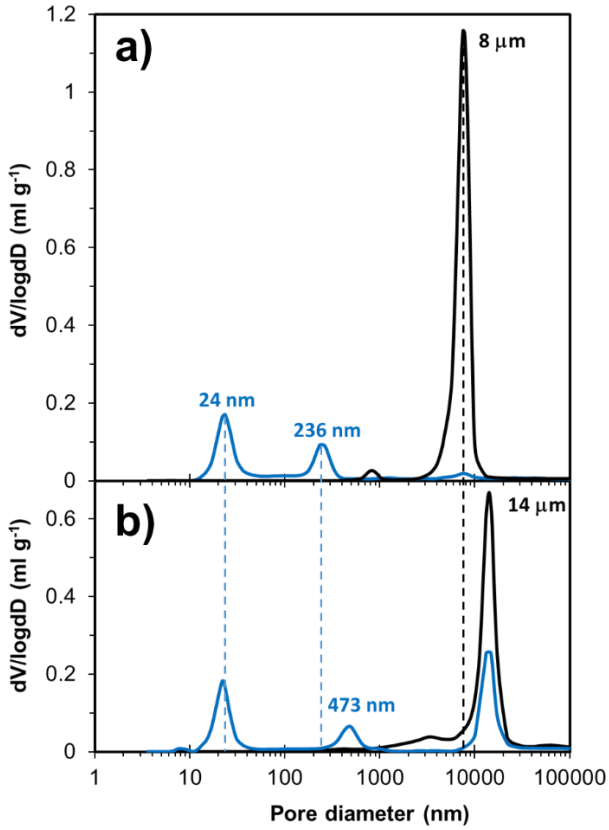

Figure SI6. Effect of the macropore size of the SiC core structure on the pore size distribution of the infiltrated SiCs monoliths. SiC made of the finer (a) or the coarser (b) particles before (black lines) and after (blue lines) infiltration

twice with 70 nm silica particles (2xSi70) and calcination at Ts-100 ºC. MIP analysis of both structures before and after double infiltration with 70 nm silica (i.e., maximum loading for SiCfs) are presented, exemplifying the effect that the initial pore size had on the pore size distribution of wash-coated monoliths.

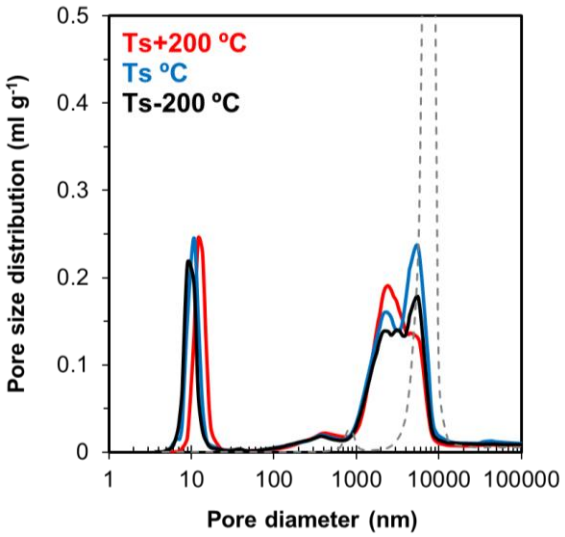

Figure SI7. Pore size distribution of SiCfs monolith infiltrated four times with colloidal alumina (4xAl) and calcined at different temperatures. The distribution of the non-infiltrated monolith is included as a reference (dashed line).

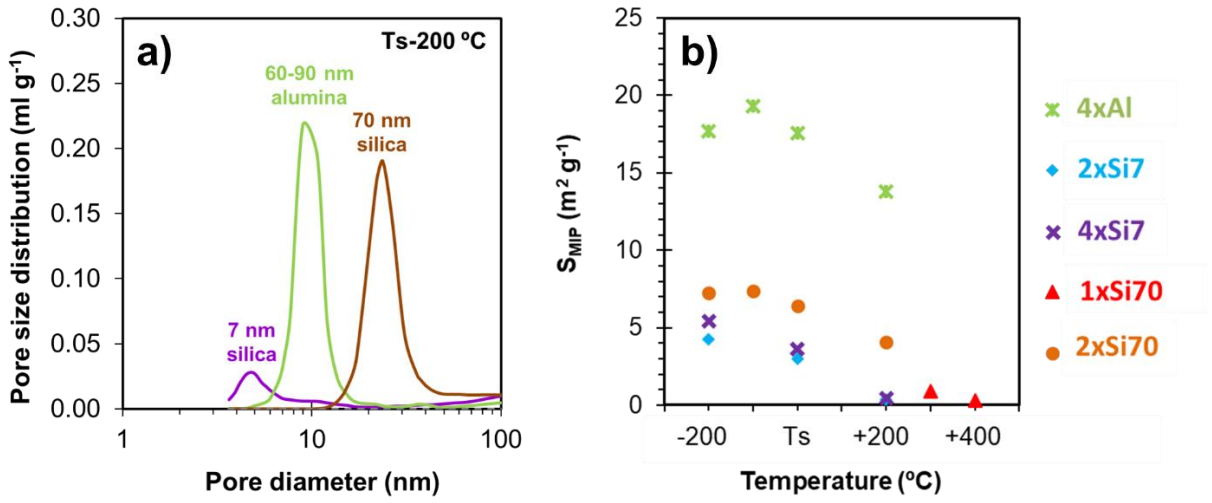

Figure SI8. Textural properties created in the SiCfs monolith by infiltration. a) Size of the interparticular voids created between the metal oxide nanoparticles at moderate calcination temperatures. b) Specific surface area generated as a function of the calcination temperature.

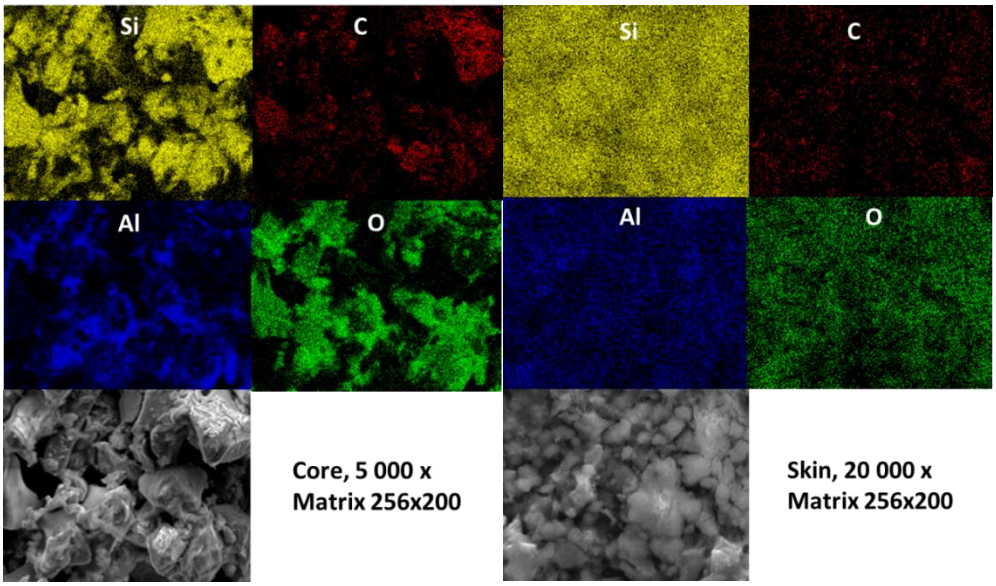

Figure SI9. EDX mapping of 4xAl-Ts SiC monolith core (left) and skin (right).

6.1 Table

Table S1. Pore volume of SiCfs and modification obtained by incorporation of silica nanoparticles into the macroporous structure.

Particle size (nm)	Wash-coat (#)	Calcination temperature (ºC)	Total pore volume (ml g^{-1})	Distribution of pores (%)		
				<50 nm	50 nm-2 μm	>2 μm
-	-	-	0.21	0	3	98
7	4	Ts-200	0.07	11	50	39
		Ts	0.07	7	72	22
		Ts+200	0.09	0	69	31
70	2	Ts-200	0.09	44	27	29
		Ts-100	0.08	48	36	16
		Ts	0.10	36	25	39

Ts+200	0.10	27	32	41

7 References

[1] G. Rothenberg, Chemical Technology. An Integral Textbook. By Andreas Jess and Peter Wasserscheid., Angew. Chemie Int. Ed. (2013). doi:10.1002/anie.201305324.

[2] J.C. Bailar, "HETEROGENIZING" HOMOGENEOUS CATALYSTS, Catal. Rev. 10 (1974) 17–36. doi:10.1080/01614947408079625.

[3] R. Fehrmann, A. Riisager, M. Haumann, Supported Ionic Liquids: Fundamentals and Applications, John Wiley & Sons, 2014. doi:10.1002/9783527654789.

[4] R.Z. Moravec, W.T. Schelling, C.F. Oldershaw, British Patent 511,556. 1939, in: Chem. Abstr, 1940: p. 7102.

[5] R.Z. Moravec, W.T. Schelling, C.F. Oldershaw, Canadian Patent 396,994. 1941, in: Chem. Abstr, 1941: p. 61031.

[6] F.G. Ciapetta, U. S. Patent 2,430,803 (1947), in: Chem. Abstr, 1948: p. 1398.

[7] A. Riisager, R. Fehrmann, M. Haumann, P. Wasserscheid, Supported Ionic Liquid Phase (SILP) Catalysis: An Innovative Concept for Homogeneous Catalysis in Continuous Fixed-Bed Reactors, Eur. J. Inorg. Chem. 2006 (2006) 695–706. doi:10.1002/ejic.200500872.

[8] J.M. Marinkovic, A. Riisager, R. Franke, P. Wasserscheid, M. Haumann, Fifteen Years of Supported Ionic Liquid Phase-Catalyzed Hydroformylation: Material and Process Developments, Ind. Eng. Chem. Res. (2019). doi:10.1021/acs.iecr.8b04010.

[9] M. Jakuttis, A. Schönweiz, S. Werner, R. Franke, K.-D. Wiese, M. Haumann, P. Wasserscheid, Rhodium–Phosphite SILP Catalysis for the Highly Selective Hydroformylation of Mixed C4 Feedstocks, Angew. Chemie Int. Ed. 50 (2011) 4492–4495. doi:10.1002/anie.201007164.

[10] H.F. Rase, Chemical reactor Design for Process Plants, Wiley New York, 1977.

[11] J.M. Herman, P.J. van den Berg, J.J.F. Scholten, The industrial hydroformylation of olefins with a rhodium-based supported liquid phase catalyst (SLPC). IV: Heat-transfer measurements in a fixed bed containing alumina SCS9 particles, Chem. Eng. J. (1987). doi:10.1016/0300-9467(87)85014-1.

[12] A.G. Machoke, T. Weissenberger, A. Inayat, A. Inayat, M. Klumpp, T. Selvam, W. Schwieger, Hierarchy concepts: classification and preparation strategies for zeolite containing materials with hierarchical porosity, Chem. Soc. Rev. (2015). doi:10.1039/c5cs00599j.

[13] J.A. Moulijn, M.T. Kreutzer, T.A. Nijhuis, F. Kapteijn, Chapter 5 - Monolithic Catalysts and Reactors: High Precision with Low Energy Consumption, in: C.G. Bruce, K. Helmut (Eds.), Adv. Catal., Academic Press, 2011: pp. 249–327. doi:http://dx.doi.org/10.1016/B978-0-12-387772-7.00005-8.

[14] P. Ávila, M. Montes, E.E. Miró, Monolithic reactors for environmental applications: A review on preparation technologies, Chem. Eng. J. 109 (2005) 11–36. doi:http://dx.doi.org/10.1016/j.cej.2005.02.025.

[15] R. Portela, V.E. García-Sánchez, M. Villarroel, S.B. Rasmussen, P. Ávila, Influence of the pore generation method on the metal dispersion and oxidation activity of supported Pt in monolithic catalysts, Appl. Catal. A Gen. 510 (2016). doi:10.1016/j.apcata.2015.10.050.

[16] G.L. Harris, Properties of Silicon Carbide, INSPEC, London, 1995.

[17] A. Dey, N. Kayal, O. Chakrabarti, Investigation of dispersion behaviour of SiC in water for slip casting of SiC, J. Ceram. Process. Res. 15 (2014) 97–101.

[18] M. Zhang, D. Jiao, G. Tan, J. Zhang, S. Wang, J. Wang, Z. Lui, Z. Zhang, R.O. Ritchie, Strong, Fracture-Resistants Biomimetic Silicon Carbide Composites with Laminated Interwoven Nanoarchitectures Inspired by the Crustancean Exoskeleton, ACS Appl. Nano Mater. 2 (2019) 1111–1119.

[19] L. Montanaro, B. Coppola, P. Palmero, J.-M. Tulliani, A review on aqueous gelcasting: A versatile and low-toxic technique to shape ceramics, Ceram. Int. 45 (2019) 9653–9673.

[20] F. Wang, D. Yao, Y. Xia, K. Zuo, J. Xu, Y. Zeng, Porous SiC ceramics prepared via freez-casting and solid state sintereing, Ceram. Int. 42 (2016) 4526–4531. doi:.1037//0033-2909.I26.1.78.

[21] F. Xue, K. Zhou, N. Wu, H. Luo, X. Wang, X. Zhou, Z. Yan, I. Abrahams, D. Zhang, Porous SiC ceramics with dendric pore structures by freeze casting chemical cross-linked polycarbosilane, Ceram. Int. 44 (2018) 6293–6299.

[22] J. Gurauskis, C.R. Graves, R. Moreno, M.I. Nieto, Self-supported ceramic substrates with directional porosity by mold freeze casting, J. Eur. Ceram. Soc. 37 (2017) 697–703. doi:10.1016/j.jeurceramsoc.2016.08.031.

[23] R.E. Chinn, K.H. Kate, S. V. Atre, Powder injection molding of silicon carbide: processing issues, Met. Powder Rep. 71 (2016) 460–464.

[24] T. Zhang, J.R.G. Evans, J. Woodthorpe, Injection Moulding of Silicon Carbide Using an Organic Vehicle Based on a Preceramic Polymer, J. Eur. Ceram. Soc. 15 (1995).

[25] H. Zhong, X. Yao, Y. Zhu, J. Zhang, D. Jiang, J. Chen, Z. Chen, X. Liu, Z. Huang, Preparation of SiC ceramics by laminated object manufacturing and pressureless sintering, J. Ceram. Sci. Technol. 6 (2015) 133–140. doi:10.4416/JCST2014-00049.

[26] P. Holtappels, B.R. Sudireddy, Ceramic Fuel Cells: Principles, Materials and Applications, in: R. Reidel, I.-W. Chen (Eds.), Ceram. Sceince Technol. Vol. 4, Wiley, 2013: pp. 345–365.

[27] P. Sajgalík, J. Sedlácek, Z. Lencés, J. Dusza, H.-T. Lin, Additive-free hot-pressed silicon carbide ceramics - A material with exceptional mechanical properties, J. Eur. Ceram. Soc. 36 (2016) 1333–1344.

[28] H.-Y. Sheng, Y.-W. Kim, I.-H. Song, Processing of silicon-derived silica-bonded silicon carbide membrane supports, Ceram. Int. 45 (2019) 2161–2169.

[29] H. Zhang, Y. Yang, B. Liu, Z. Huang, The preparation of SiC-based ceramics by one novel strategy combined 3D printing technology and liquid silicon infilitration process, Ceram. Int. 45 (2019) 10800–10804.

[30] Z. Chen, Z. Li, J. Li, C. Liu, C. Lao, Y. Fu, C. Liu, Y. Li, P. Wang, Y. He, 3D printing of ceramics: A review, J. Eur. Ceram. Soc. 39 (2019) 661–687. doi:10.1016/j.jeurceramsoc.2018.11.013.

[31] P. Sánchez, F. de la Osa, Ana Raquel Dorado, J.M. Garcia-Vargas, Silica-based catalysts for fuel applications, in: Chem. Silica Zeolite-Based Mater. Vol. 2, 2019: pp. 143–161.

[32] A. Riisager, P. Wasserscheid, R. Van Hal, R. Fehrmann, Continuous fixed-bed gas-phase hydroformylation using supported ionic liquid-phase (SILP) Rh catalysts, J. Catal. (2003). doi:10.1016/S0021-9517(03)00223-9.

[33] M. Trueba, S.P. Trasatti, γ -Alumina as a Support for Catalysts : A Review of Fundamental Aspects, (2005) 3393–3403. doi:10.1002/ejic.200500348.

[34] M. Logemann, J.M. Marinkovic, M. Schörner, E.J. García-Suárez, C. Hecht, R. Franke, M. Wessling, A. Riisager, R. Fehrmann, M. Haumann, Continuous gas-phase hydroformylation of 1-butylene in a membrane reactor by supported liquid-phase (SLP) catalysis, Submitted. (2019).

[35] P. Stobbe, U. Haok, Porous ceramic body and method for production thereof, US 2006/0236668A1, 2006.

[36] J. Hoffmann Jørgensen, A method of producing a ceramic support and a ceramic support, PA 2019 01472, 2020.

[37] S.M. Dutczak, M.W.J. Luiten-Olieman, H.J. Zwijnenberg, L. a M. Bolhuis-Versteeg, L. Winnubst, M. a. Hempenius, N.E. Benes, M. Wessling, D. Stamatialis, Composite capillary membrane for solvent resistant nanofiltration, J. Memb. Sci. 372 (2011) 182–190. doi:10.1016/j.memsci.2011.01.058.

[38] N. Stafie, D.F. Stamatialis, M. Wessling, Insight into the transport of hexane-solute systems through tailor-made composite membranes, J. Memb. Sci. 228 (2004) 103–116. doi:10.1016/j.memsci.2003.10.002.

[39] E.W. Washburn, The Dynamics of Capillary Flow, Phys. Rev. 17 (1921) 273–283. doi:http://dx.doi.org/10.1103/PhysRev.17.273.

[40] K.K. Unger, C. du Fresne von Hohenesche, M. Schulte, Columns, Packings and Stationary Phases, in: Prep. Chromatogr., Wiley-VCH Verlag GmbH & Co. KGaA, Weinheim, FRG, 2005: pp. 51–105. doi:10.1002/3527603484.ch3.

[41] C.S. Chang, Y. Deng, A nonlinear packing model for multi-sized particle mixtures, Powder Technol. 336 (2018) 449–464.

[42] R. Terry, K. Baker, In-Situ Electron Microscopy Studies of Catalyst Deactivation, Stud. Surf. Sci. Catal. 68 (1991) 1–27. doi:10.1016/S0167-2991(08)62618-X.

[43] S. Tian, J. Jiang, F. Yan, K. Li, X. Chen, Synthesis of Highly Efficient CaO-Based, Self-Stabilizing CO2 Sorbents via Structure-Reforming of Steel Slag, Environ. Sci. & Technol. 49 (2015) 7464–7472. doi:10.1021/acs.est.5b00244.

[44] J. Phromprasit, J. Powell, S. Assabumrungrat, Metals (Mg, Sr and Al) modified CaO based sorbent for CO2 sorption/desorption stability in fixed bed reactor for high temperature application, Chem. Eng. J. 284 (2016) 1212–1223. doi:10.1016/J.CEJ.2015.09.038.

[45] R.W. Baker, Membrane Technology and Applications, 2012. doi:10.1016/S0958-2118(96)90133-0.

[46] T.C. Merkel, R.P. Gupta, B.S. Turk, B.D. Freeman, Mixed-gas permeation of syngas components in poly (dimethylsiloxane) and poly (1-trimethylsilyl-1-propyne) at elevated temperatures, J. Memb. Sci. 191 (2001) 85–94.

[47] L. Landau, B. Levich, Dragging of a Liquid by a Moving Plate, in: Dyn. Curved Front., 1988: pp. 141–153. doi:10.1016/b978-0-08-092523-3.50016-2.

[48] G.J. Van Amerongen, The permeability of different rubbers to gases and its relation to diffusivity and solubility, J. Appl. Phys. 17 (1946) 972–985. doi:10.1063/1.1707667.

[49] J.G. Wijmans, R.W. Baker, The solution-diffusion model: a review, J. Memb. Sci. 107 (1995) 1–21. doi:10.1016/0376-7388(95)00102-I.

[50] L. Hu, J. Cheng, Y. Li, J. Liu, J. Zhou, K. Cen, Optimization of coating solution viscosity

of hollow fiber-supported polydimethylsiloxane membrane for CO2/H2separation, J. Appl. Polym. Sci. 135 (2018) 1–10. doi:10.1002/app.45765.